

Partial molecular orbitals in face-sharing 3d manganese trimer: Comparative studies on Ba₄TaMn₃O₁₂ and Ba₄NbMn₃O₁₂

Anzar Ali ^{1,2,*}, Heung-Sik Kim ^{3,*}, Poonam Yadav ^{1,2}, Suheon Lee,^{1,2} Duhee Yoon,^{1,4} and Sungkyun Choi ^{1,2,†}

¹Center for Integrated Nanostructure Physics, Institute for Basic Science, Suwon 16419, Republic of Korea

²Sungkyunkwan University, Suwon 16419, Republic of Korea

³Department of Physics and Institute of Quantum Convergence Technology, Kangwon National University, Chuncheon 24341, Republic of Korea

⁴Department of Energy Science, Sungkyunkwan University, Suwon 16419, Republic of Korea



(Received 16 March 2023; accepted 22 December 2023; published 4 March 2024)

We present a molecular orbital candidate Ba₄TaMn₃O₁₂ with a face-sharing octahedra trimer, by comparing it with a related compound Ba₄NbMn₃O₁₂. The synthesis of the polycrystalline powder is optimized by suppressing the secondary impurity phase via x-ray diffraction. Magnetic susceptibility measurements on the optimized samples reveal a weak magnetic hysteresis with magnetic transitions consistent with heat capacity results. The effective magnetic moments from susceptibility indicate a strongly coupled $S = 2$ antiferromagnetic trimer at around room temperature, whereas the estimated magnetic entropy from heat capacity suggests the localized $S = 3/2$ trimer. These results can be explainable by a partial molecular orbital state, in which three t_{2g} electrons are localized in each Mn ion and one e_g electron is delocalized over two-end Mn ions of the trimer based on density functional theory calculations. This unconventional 3d orbital state is comprehended as a consequence of competition between the hybrid interatomic orbitals within the Mn trimer and the local moment formation by on-site Coulomb correlations.

DOI: [10.1103/PhysRevResearch.6.013231](https://doi.org/10.1103/PhysRevResearch.6.013231)

I. INTRODUCTION

A Mott state [1] has been studied extensively for understanding the electronic state of correlated electron systems stabilized by the competition between the electron correlation energy and other energy scales, such as spin-orbit coupling and crystalline electric fields. Quantum magnets containing transition metal (TM) ions can be generally understood in the localized electron scheme by learning the properties of the single magnetic ion and the exchange interactions with its surrounding magnetic ions in a given structural motif.

More recently, new electronic states have attracted significant interest in discovering novel electronic properties. Such an example is a molecular orbital state (MO) [2], where electrons are delocalized and shared by several magnetic ions nearby, which cannot be described by a simple single-ion localized electron picture. It has been demonstrated that this unconventional phase can be realized in heavy TM-based compounds, such as the 4d trimer Ba₄Ru₃O₁₀ [3,4] and 5d trimer Ba₅CuIr₃O₁₂ [5] by the interplay between spin-orbit coupling and extended d orbitals. In these compounds, the TM octahedra form a linear trimer via a face-sharing geometry, which enables an unusually short distance between TM ions,

allowing a sizable direct overlap of d orbitals. As a result, they can stabilize the MO state.

However, little is known about the MO state from 3d TM-based compounds. It is generally recognized that characters of 3d orbitals are very different from those of 4d and 5d orbitals. For instance, the spin-orbit coupling is reduced in 3d orbitals and electrons are significantly more localized, leading to large electronic Coulomb interactions. In contrast, 3d materials have a higher Hund's coupling energy, which is associated with an intra-atomic exchange in multiorbital systems [6]. This distinct energy hierarchy in 3d TM ions compared to those in 4d and 5d counterparts could render the MO state from 3d materials unusual. Therefore, the interplay between spin-orbit and Hund's coupling of 3d compounds could provide the opportunity to discover novel characters of the MO state.

In this regard, a recently reported hexagonal perovskite Ba₄NbMn₃O₁₂ [7] is intriguing. This compound also contains the linear trimer with a three face-sharing MnO₆ octahedra, which allows a much closer Mn-Mn distance (~ 2.47 Å) than the one encountered in common corner-sharing geometries [8]. It is comparable to that of an Mn metal (~ 2.48 Å [9]). Thus this structural motif could enable a strong direct overlap between 3d orbitals. Nonetheless, Ba₄NbMn₃O₁₂ is an insulator, which suggests an unconventional electronic structure in 3d orbitals. Indeed, magnetic susceptibility measurements uncovered the intriguing magnetic properties of Ba₄NbMn₃O₁₂ [7], such as that the effective magnetic moment extracted from high temperatures corresponded to only $S = 2$ from the trimer, which is expected to be a combination of two Mn⁴⁺ ions and one Mn³⁺ ion. Based on this, a magnetically ordered

*These authors contributed equally to this work.

†sungkyunchoi@skku.edu

Published by the American Physical Society under the terms of the [Creative Commons Attribution 4.0 International](https://creativecommons.org/licenses/by/4.0/) license. Further distribution of this work must maintain attribution to the author(s) and the published article's title, journal citation, and DOI.

state within the trimer was suggested even at 300 K [7] even if the long-range magnetic ordering temperature can be lower than 42.4 K.

To understand the magnetic ground state of $\text{Ba}_4\text{NbMn}_3\text{O}_{12}$ based on the expected mixed valent state of Mn^{3+} and Mn^{4+} , two hypothetical models [7] in the localized electron scheme are proposed: (i) two parallel moments from Mn^{4+} ions and one antiparallel moment from Mn^{3+} ion ($3d^4$, $S = 1$ for low spin); (ii) two antiparallel moments from Mn^{4+} ions and one moment from Mn^{3+} ion ($3d^4$, $S = 2$ for high spin). Note that the spin of Mn^{4+} ions in both models is the same ($3d^3$, $S = 3/2$).

However, the reported heat capacity [7] disagrees with both models and reveals a significantly lower magnetic entropy for the $S = 2$ system than expected. Thus the consistent characterization of carefully grown samples needs to be done, compared to detailed theoretical calculations using the suggested magnetic structures. In addition, it is crucial to conduct a comparative study to better understand the peculiar electronic properties of $\text{Ba}_4\text{NbMn}_3\text{O}_{12}$ by synthesizing and examining a related compound if possible.

Herein, we present the synthesis and characterization of a $3d$ trimer $\text{Ba}_4\text{TaMn}_3\text{O}_{12}$ and an improved sample quality of its related compound $\text{Ba}_4\text{NbMn}_3\text{O}_{12}$. The growth optimization is made by controlling an amount of volatile MnO_2 powder, monitored by x-ray diffraction refinements. Sharp phonon peaks observed by Raman scattering corroborate the high quality of our samples. We confirm tiny magnetic hysteresis anomalies and find signatures of magnetic transitions in both compounds in magnetic susceptibility measurements, compatible with heat capacity experiments. The effective magnetic moments from susceptibility indicate a strongly coupled $S = 2$ antiferromagnetic trimer at around room temperature, whereas the estimated magnetic entropy from heat capacity suggests the localized $S = 3/2$ moments in the trimer. *Ab initio* calculations find that the localized electrons at $\text{Mn } t_{2g}$ orbitals and the delocalized electron at $\text{Mn } e_g$ orbitals spread over two-end Mn ions of the trimer, which explains both susceptibility and heat capacity results. Hence we propose a partial molecular orbital, which is the coexistent state of localized electrons and molecular orbitals in $\text{Ba}_4\mathcal{M}\text{Mn}_3\text{O}_{12}$ ($\mathcal{M} = \text{Ta, Nb}$). This peculiar state is interpreted by the result of the competition between the hybrid interatomic orbitals within the Mn trimer and the local moment formation by on-site Coulomb correlations. Further, we discuss the possible relevance of this trimer-based material platform in searching for the insulator-metal transition that might be useful in developing innovative magnetic devices.

The rest of the paper is organized as follows. The experimental and calculational details are shown in Secs. II and III, respectively. The optimization of the polycrystalline powder is explained in Sec. IV A. Refined crystal structures by x-ray diffraction are presented in Sec. IV B. Sections IV C and IV D present magnetic susceptibility and heat capacity results, respectively. Resistivity results are given in Sec. IV E. Raman spectra are compared in Sec. IV F, followed by *ab initio* calculations in Sec. V. Our results are discussed based on reported references in Sec. VI and, finally, conclusions are given in Sec. VII. The Appendix provides results from nonmagnetic DFT calculations.

II. EXPERIMENTAL DETAILS

The polycrystalline samples of $\text{Ba}_4\mathcal{M}\text{Mn}_3\text{O}_{12}$ ($\mathcal{M} = \text{Ta, Nb}$) were synthesized using a solid-state reaction. The starting precursors of BaCO_3 (Alfa Aesar, 99.95 %), $\mathcal{M}_2\text{O}_5$ ($\mathcal{M} = \text{Ta, Nb}$) (Kojundo, 99.9 %), and MnO_2 (Kojundo, 99.99 %) were taken in stoichiometric ratio and ground well in an agate mortar using a pestle. Mixed powders were calcined at 900°C for 24 h. After the calcination, the powders were repeatedly reground, pelletized, and sintered for 24 hrs at 1100°C , 1300°C , and 1420°C . Slightly modified conditions were also used—the calcination at 1100°C , followed by the subsequent sintering at 1200°C and 1420°C for 24 h at each temperature. Note that our optimized batches were synthesized using the modified condition. The excess of starting MnO_2 powder was also added to compensate for its evaporation, effectively suppressing the impurity phase formation.

The phase purity of polycrystalline powder was confirmed using x-ray diffraction measurements at room temperature using a Rigaku SmartLab X-ray Diffractometer. The high-quality XRD data were collected from a Rigaku D8 advance high-resolution x-ray diffractometer using a Bragg-Brentano geometry with a $\text{Cu } K\alpha_{1,2}$ source, presented in this paper. A JANA2006 software [10] was used for Rietveld refinements to determine the crystal structures.

Magnetic susceptibility experiments for zero-field-cooled (ZFC) and field-cooled (FC) measurements were performed with a Physical Property Measurement System (PPMS, Dynacool, Quantum Design) equipped with a vibrating sample magnetometry module between 300 and 2 K with a magnetic field of 0.01 T or 0.1 T. Magnetization measurements were done in the magnetic field from -7 to 7 T at 2, 30, 50, 70, and 100 K.

Heat capacity measurements were carried out with a PPMS at $H = 0$ and 9 T from 160 to 2 K. Before each measurement, the addenda was measured using the same temperature range by the thermal relaxation method. Addenda heat capacities were subtracted from total heat capacities to obtain the sample heat capacity as usual.

Electrical resistance was measured on sintered rectangular pellets using a PPMS between 260 and 390 K. The rectangular pellets of $3 \times 6 \text{ mm}^2$ dimensions were prepared using a rectangular die set. A four-probe method was utilized, where the electrical contacts were made using gold wires and silver epoxy. Measured resistance was converted to resistivity using the length and area of the cross section.

Raman measurements were performed using the 514.5 nm line of an Ar-ion laser as the excitation source at room temperature. The laser beam was focused onto the sample through a $50\times$ objective lens (numerical aperture = 0.8) in a backscattering geometry. The laser power was kept at 0.5 mW to minimize the local beam heating. The Raman signals were recorded with a liquid-nitrogen-cooled charge-coupled-device detector after dispersion by a Horiba iHR550 spectrometer (2400 grooves/mm).

III. COMPUTATIONAL DETAILS

The Vienna *ab initio* simulation package (VASP) [11,12] was employed for electronic structure calculations, with 400 eV of plane-wave energy cutoff and $5 \times 5 \times 2$ k -point

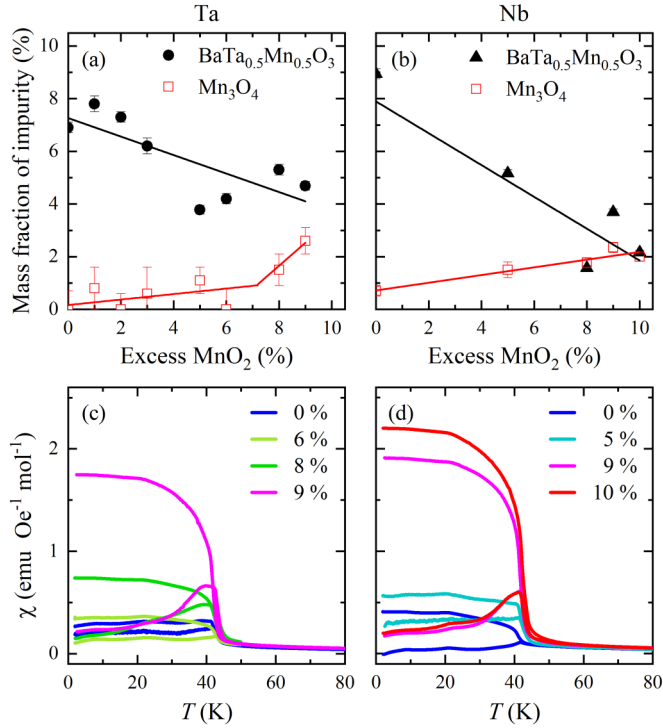


FIG. 1. Optimization of polycrystalline growths of $\text{Ba}_4\mathcal{M}\text{Mn}_3\text{O}_{12}$ ($\mathcal{M} = \text{Ta}, \text{Nb}$). (a), (b) Evolution of the mass fraction of the unwanted impurity phase, $\text{BaTa}_{0.5}\text{Mn}_{0.5}\text{O}_3$ and $\text{BaNb}_{0.5}\text{Mn}_{0.5}\text{O}_3$, and Mn_3O_4 , upon an excess of MnO_2 starting powder. Error bars from the refinement are also given. (c), (d) Selected magnetic susceptibility for $\text{Ba}_4\text{TaMn}_3\text{O}_{12}$ and $\text{Ba}_4\text{NbMn}_3\text{O}_{12}$ at $H = 0.01$ T, respectively.

sampling for conventional hexagonal unit cells. A revised Perdew-Burke-Ernzherof generalized gradient approximation for solids (PBEsol) was used to approximate the exchange-correlation functional. The strong Coulomb repulsion within the Mn sites was further treated with a simplified rotationally invariant flavor of density functional theory (DFT)+ U_{eff} [13], where the effective on-site Coulomb repulsion $U_{\text{eff}} \equiv U - J$ was set to 4 eV for the Mn d orbital. Note that the value of $U_{\text{eff}} = 4$ eV was widely adopted for a range of Mn compounds [14–17] and reported to produce reasonable results.

IV. EXPERIMENTS

A. Optimization of polycrystalline growths

We found the unwelcome impurity phase, $\text{Ba}\mathcal{M}_{0.5}\text{Mn}_{0.5}\text{O}_3$ ($\mathcal{M} = \text{Ta}, \text{Nb}$), by x-ray diffraction during the synthesis of $\text{Ba}_4\text{TaMn}_3\text{O}_{12}$ and $\text{Ba}_4\text{NbMn}_3\text{O}_{12}$ polycrystalline samples. Thus we optimized our growths by controlling the amount of the excess MnO_2 starting powder to compensate for its evaporation during the reaction.

Figure 1 presents the mass fraction of the impurity phase extracted by the structural refinements using x-ray diffraction measurements, followed by magnetic susceptibility measurements. As shown in Fig. 1(a), the mass fraction of the impurity phase linearly decreases with an excess of MnO_2 , reaching a minimum value when the 9% (10%) of excessive MnO_2 powder is initially added for $\text{Ba}_4\text{TaMn}_3\text{O}_{12}$ ($\text{Ba}_4\text{NbMn}_3\text{O}_{12}$)

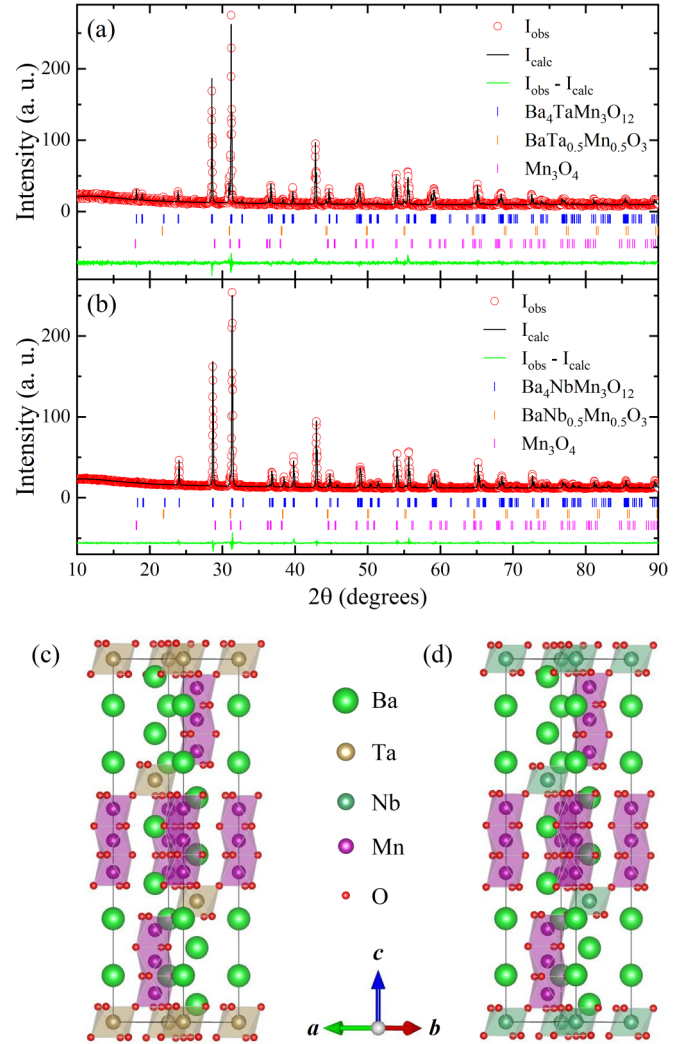


FIG. 2. (a), (b) Structural refinements using the powder x-ray diffraction data collected at room temperature from $\text{Ba}_4\text{TaMn}_3\text{O}_{12}$ and $\text{Ba}_4\text{NbMn}_3\text{O}_{12}$, respectively. (c), (d) Refined crystal structures. The Mn trimer is indicated by shaded purple polyhedra along the crystallographic c axis.

before the first sintering. We found that the magnetic susceptibility splitting ($\chi_{\text{FC}} - \chi_{\text{ZFC}}$) at 2 K is bigger for such batches, as shown in Figs. 1(c) and 1(d) for $\text{Ba}_4\text{TaMn}_3\text{O}_{12}$ and $\text{Ba}_4\text{NbMn}_3\text{O}_{12}$, respectively. We studied the structural, magnetic, thermal, electric, and optic properties using the optimized batch of each compound in this paper. We also found a tiny mass fraction of the secondary impurity phase Mn_3O_4 ($\sim 2\%$) towards a higher excess of MnO_2 , as shown in Figs. 1(a) and 1(b).

B. Crystal structure

To determine the crystal structure of $\text{Ba}_4\mathcal{M}\text{Mn}_3\text{O}_{12}$ ($\mathcal{M} = \text{Ta}, \text{Nb}$) compounds, powder x-ray diffraction was performed, revealing the high quality of the sample. Consequently, these batches were used for the subsequent characterization measurements presented in this paper. Figure 2 shows the x-ray diffraction patterns of $\text{Ba}_4\text{TaMn}_3\text{O}_{12}$ and $\text{Ba}_4\text{NbMn}_3\text{O}_{12}$ samples collected at room temperature.

TABLE I. Refined structural parameters for $\text{Ba}_4\text{TaMn}_3\text{O}_{12}$ at 300 K. Space group $R\bar{3}m$, No. 166, $a = 5.72543(12)$ Å, $c = 28.14875(87)$, U_{iso} (fixed) = 0.001 Å², goodness of fit (GOF) = 1.08, $R_p = 7.33\%$, and $wR_p = 9.25\%$. Mass fraction of $\text{BaTa}_{0.5}\text{Mn}_{0.5}\text{O}_3 = 4.69(16)\%$ and $\text{Mn}_3\text{O}_4 = 2.6(5)\%$. Sites are assumed to be fully occupied.

Atom	Site	x	y	z
Ba1	6c	0	0	0.1282(3)
Ba2	6c	0	0	0.2848(2)
Ta1	3a	0	0	0
Mn1	3b	0	0	0.5
Mn2	6c	0	0	0.4131(6)
O1	18h	0.486(2)	0.514(2)	0.1270(9)
O2	18h	0.489(3)	0.511(3)	0.2912(11)

Rietveld refinements confirmed that both $\text{Ba}_4\text{TaMn}_3\text{O}_{12}$ and $\text{Ba}_4\text{NbMn}_3\text{O}_{12}$ crystallized in a trigonal crystal structure ($R\bar{3}m$, No. 166), consistent with the previous research [7] on $\text{Ba}_4\text{NbMn}_3\text{O}_{12}$. A minor impurity phase [$\sim 3\%$ of disordered perovskite $\text{Ba}\mathcal{M}_{0.5}\text{Mn}_{0.5}\text{O}_3$ ($\mathcal{M} = \text{Ta}, \text{Nb}$)] was identified in both compounds, which was also reported previously for $\text{Ba}_4\text{NbMn}_3\text{O}_{12}$ [7]. Figures 2(c) and 2(d) illustrate the refined crystal structures, where three MnO_6 octahedra are connected by their faces and form a Mn_3O_{12} trimer. The Mn trimers are alternatively connected by corner-sharing nonmagnetic TaO_6 or NbO_6 octahedra by forming 12 hexagonal layers in total within the unit cell. The extracted structural parameters of $\text{Ba}_4\text{TaMn}_3\text{O}_{12}$ and $\text{Ba}_4\text{NbMn}_3\text{O}_{12}$ are provided in Table I and Table II, respectively. Note that we found only a few percentages of the site mixing between Mn and Ta (Nb) sites.

C. Magnetic susceptibility

Magnetic susceptibility and magnetization measurements were then performed to understand the magnetism of $\text{Ba}_4\text{TaMn}_3\text{O}_{12}$ and $\text{Ba}_4\text{NbMn}_3\text{O}_{12}$. Figures 3(a) and 3(b) show the temperature-dependent ZFC and FC magnetic susceptibility data [$\chi(T) = M/H$, where M is the magnetization and H is the applied magnetic field] measured at $H = 0.1$ T from 300 K to 2 K, whereas Figs. 3(c) and 3(d) exhibit their inverse magnetic susceptibilities. Magnetic susceptibility data demonstrated Curie-Weiss-like behaviors at

TABLE II. Refined structural parameters for $\text{Ba}_4\text{NbMn}_3\text{O}_{12}$ at 300 K. Space group $R\bar{3}m$, No. 166, $a = 5.72996(4)$ Å, $c = 28.16229(27)$, U_{iso} (fixed) = 0.001 Å², goodness of fit (GOF) = 1.27, $R_p = 2.55\%$, and $wR_p = 3.27\%$. Mass fraction of $\text{BaNb}_{0.5}\text{Mn}_{0.5}\text{O}_3 = 2.17(6)\%$ and $\text{Mn}_3\text{O}_4 = 2.00(18)\%$. Sites are assumed to be fully occupied.

Atom	Site	x	y	z
Ba1	6c	0	0	0.1292(1)
Ba2	6c	0	0	0.2846(1)
Nb	3a	0	0	0
Mn1	3b	0	0	0.5
Mn2	6c	0	0	0.4103(2)
O1	18h	0.489(1)	0.511(1)	0.1252(3)
O2	18h	0.490(1)	0.510(1)	0.2953(4)

high temperatures, but $\chi(T)$ was sharply increased below 43.72 K and 42.42 K for $\text{Ba}_4\text{TaMn}_3\text{O}_{12}$ and $\text{Ba}_4\text{NbMn}_3\text{O}_{12}$, respectively, consistent with the anomaly found in $d\chi(T)/dT$ [insets of Figs. 3(a) and 3(b)]. Below those temperatures, labeled as T_1 , we observed bifurcations in the ZFC and FC data, consistent with a hysteresis loop that was clearly seen in $M(H)$ [Figs. 3(e)–3(h)]. As shown in Figs. 3(g) and 3(h), the magnetic moments at 2 K with 7 T are $1.32 \mu_B/\text{f.u.}$ for $\text{Ba}_4\text{TaMn}_3\text{O}_{12}$ and $1.53 \mu_B/\text{f.u.}$ for $\text{Ba}_4\text{NbMn}_3\text{O}_{12}$, suggesting that more measurements would be needed at higher magnetic fields. We found additional anomalies at 29.77 K and 23.5 K for $\text{Ba}_4\text{TaMn}_3\text{O}_{12}$ and $\text{Ba}_4\text{NbMn}_3\text{O}_{12}$, respectively, which were also visible in $d(\chi T)/dT$ (Fig. 6).

The $\chi^{-1}(T)$ data between 100 and 370 K were fitted using the Curie-Weiss (CW) equation, $\chi(T) = \chi_0 + C/(T - \theta)$, where χ_0 is temperature-independent susceptibility, C is the Curie constant, and θ is the CW temperature, as summarized in Tables III and IV. The effective magnetic moment was calculated using $\mu_{\text{eff}} = \sqrt{3k_B C/N_A}$ [18], where N_A is the Avogadro constant and k_B is the Boltzmann constant. Our fitting results in the temperature range between 100 and 275 K showed that $\mu_{\text{eff}} = 4.72$ (4.87) μ_B for $\text{Ba}_4\text{TaMn}_3\text{O}_{12}$ ($\text{Ba}_4\text{NbMn}_3\text{O}_{12}$), which is consistent with both a previous report on $\text{Ba}_4\text{NbMn}_3\text{O}_{12}$ [7] and the expected $4.9 \mu_B$ from two magnetic structural candidates with the $S = 2$ trimer, which was proposed for $\text{Ba}_4\text{NbMn}_3\text{O}_{12}$ [7]. Also, a positive temperature-independent susceptibility $\chi_0 = 3.15 \times 10^{-3}$ (2.06×10^{-3}) emu Oe⁻¹mol⁻¹ for $\text{Ba}_4\text{TaMn}_3\text{O}_{12}$ ($\text{Ba}_4\text{NbMn}_3\text{O}_{12}$) is similar to that reported in $\text{Ba}_4\text{NbMn}_3\text{O}_{12}$ [7], reminiscent of the van Vleck paramagnetism [19].

These two observations are compatible with an idea of locally aligned magnetic moments even at high temperatures with remnant susceptibility [7] after the local moments are established within the trimer. It could be contributed from the mixing between the ground and excited states [20] within the Mn trimer in $\text{Ba}_4\mathcal{M}\text{Mn}_3\text{O}_{12}$. Thus all moments are not freely fluctuating, but the local antiferromagnetic moment within the trimer is already formed even at room temperature, which will not contribute to the Curie-Weiss temperature. This means that the positive Curie temperature reflects the subdominant ferromagnetic exchange interaction. In this view, the extracted parameters can be interpreted with the trimer unity rather than individual spins of Mn. This picture is also consistent with the localized part ($S = 3/2$) of the extracted effective moment. The delocalized part ($S = 1/2$) will be discussed soon. In $\text{Ba}_4\mathcal{M}\text{Mn}_3\text{O}_{12}$, the Curie-Weiss temperature is positive, which indicates the effective ferromagnetic intertrimer coupling. We note that positive values of χ_0 are also observed in other related compounds, such as $\text{Ba}_4\text{NbMn}_3\text{O}_{12}$ [7], $\text{Ba}_4\text{NbRu}_3\text{O}_{12}$ [21], and $\text{Ba}_4\text{Nb}_{0.8}\text{Ir}_{3.2}\text{O}_{12}$ [22]. We also tried the Curie-Weiss fit without the χ_0 term (not shown), but this gave completely nonphysical results, such as wrong effective magnetic moments. Thus the sizable temperature-independent paramagnetic term is essential for reliable fits to extract the physically sensible parameters for $\text{Ba}_4\mathcal{M}\text{Mn}_3\text{O}_{12}$.

For a more systematic analysis, we also performed the CW fits with a different range of temperatures, as summarized in Table III and Table IV for $\text{Ba}_4\text{TaMn}_3\text{O}_{12}$ and $\text{Ba}_4\text{NbMn}_3\text{O}_{12}$, respectively. The effective magnetic moments are comparable

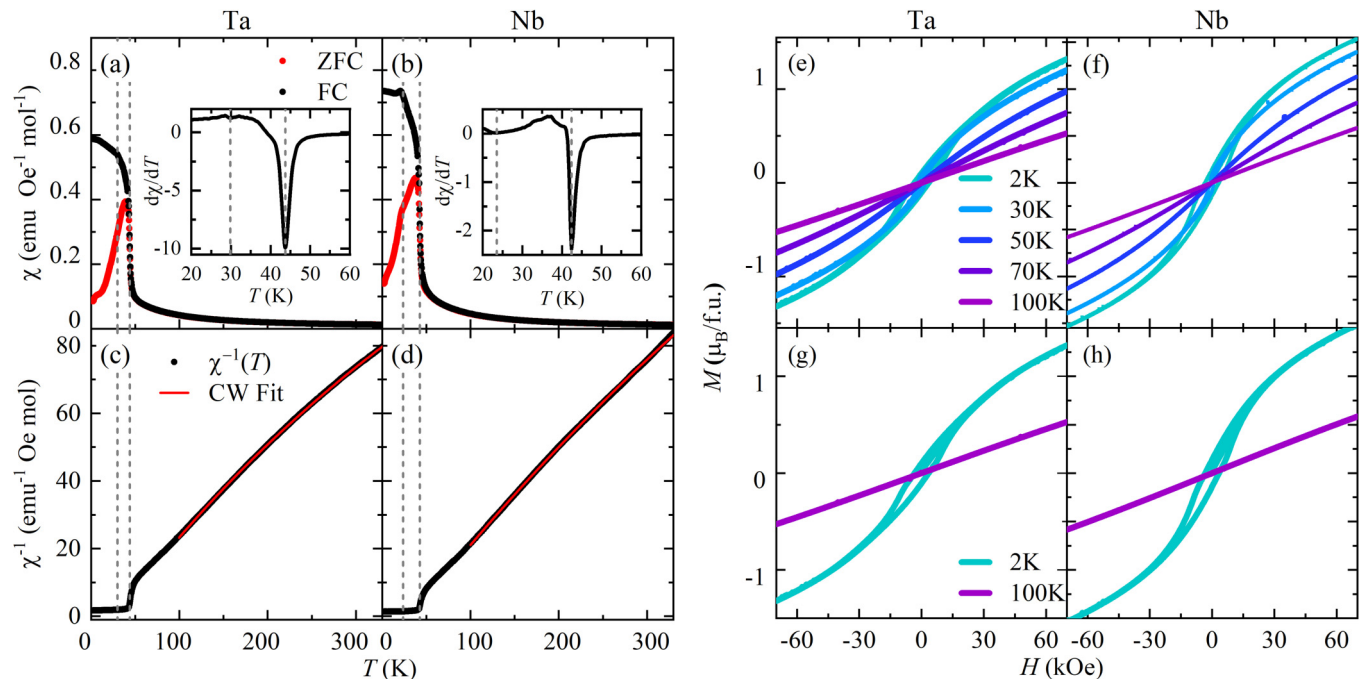


FIG. 3. (a), (b) Magnetic susceptibility collected at $H = 0.1$ T. Insets: the first derivative of magnetic susceptibility revealed anomalous temperatures at 43.72 K (42.42 K) for T_1 and 29.77 K (23.5 K) for T_2 for $\text{Ba}_4\text{TaMn}_3\text{O}_{12}$ ($\text{Ba}_4\text{NbMn}_3\text{O}_{12}$), respectively. (c), (d) Inverse magnetic susceptibilities (solid black lines) and Curie-Weiss (CW) fits (solid red lines). The gray dashed vertical lines illustrate the anomalous temperatures consistently found in (a)–(d). (e), (f) Magnetization (M) with magnetic field (H) of $\text{Ba}_4\text{TaMn}_3\text{O}_{12}$ and $\text{Ba}_4\text{NbMn}_3\text{O}_{12}$ measured at various temperatures (T) between -70 and 70 kOe. (g), (h) $M(H)$ data at 2 and 100 K.

and θ values fluctuate in all trials in $\text{Ba}_4\text{TaMn}_3\text{O}_{12}$. This means that the antiferromagnetically coupled moments within the trimer are robust up to 370 K for $\text{Ba}_4\text{TaMn}_3\text{O}_{12}$ by giving the compatible, effective magnetic moment with that of $\text{Ba}_4\text{NbMn}_3\text{O}_{12}$ from Ref. [7].

On the other hand, the reported CW parameters in the literature [7] are somewhat different from our parameters from $\text{Ba}_4\text{NbMn}_3\text{O}_{12}$, as compared in Table IV. The effective moments extracted from fits in $\text{Ba}_4\text{NbMn}_3\text{O}_{12}$ show an increasing trend as the lower bound of the fitted temperature becomes higher. Also, the CW temperatures become more negative simultaneously, consistent with the trend of the χ_0 values. These behaviors of χ_0 and μ_{eff} signal that the three Mn spins behave more independently towards higher temperatures in $\text{Ba}_4\text{NbMn}_3\text{O}_{12}$, unlike $\text{Ba}_4\text{TaMn}_3\text{O}_{12}$. The fitting parameters χ_0 and μ_{eff} for both $\text{Ba}_4\text{Mn}_3\text{O}_{12}$ are consistent with results from Ref. [7] when the fitting was done in the identical

temperature range (between 100 and 275 K). Interestingly, the effective magnetic moment extracted from $\text{Ba}_4\text{NbMn}_3\text{O}_{12}$ at the higher temperature range is comparable to the values expected when all moments freely respond to the external magnetic field in the trimer unit having two Mn^{+4} ions and one Mn^{+3} ion; for instance, 6.16 (for the low-spin model) or 7.35 (for the high-spin model) $\mu_B/\text{f.u.}$ [7]. As the temperature is lowered, the three Mn spins form the antiferromagnetic trimer even above the long-range magnetic ordering temperature and yield the effective magnetic moment, comparable to the $S = 2$ system. These results suggest that the bonding of Mn spins in the trimer is stronger for $\text{Ba}_4\text{TaMn}_3\text{O}_{12}$ than $\text{Ba}_4\text{NbMn}_3\text{O}_{12}$. Accordingly, a similar behavior for χ_0 and μ_{eff} is expected for $\text{Ba}_4\text{TaMn}_3\text{O}_{12}$ at higher temperatures above 370 K. We note that Ref. [7] proposed the ferrimagnetic transition behavior from $\chi(T)$ with a negative θ value for $\text{Ba}_4\text{NbMn}_3\text{O}_{12}$, which means the dominant antiferromagnetic intertrimer interaction. However, we did not observe such a

TABLE III. Parameters obtained from CW fits using the inverse magnetic susceptibility $\chi^{-1}(T)$ of $\text{Ba}_4\text{TaMn}_3\text{O}_{12}$. θ is the CW temperature. C ($\text{emu K Oe}^{-1}\text{mol}^{-1}$) is the Curie constant. χ_0 ($\text{emu Oe}^{-1}\text{mol}^{-1}$) is the temperature-independent magnetic susceptibility. μ_{eff} is the effective magnetic moment.

Range (K)	$\chi_0 (\times 10^{-3})$	θ (K)	C	$\mu_{\text{eff}} (\mu_B)$
370–300	3.24	23.14	2.86027	4.78
370–200	3.73	40.14	2.55749	4.52
370–100	3.14	28.78	2.83327	4.76
275–100	3.15	31.61	2.78916	4.72

TABLE IV. Parameters obtained from CW fits using the inverse magnetic susceptibility $\chi^{-1}(T)$ of $\text{Ba}_4\text{NbMn}_3\text{O}_{12}$.

Range (K)	$\chi_0 (\times 10^{-3})$	θ (K)	C	$\mu_{\text{eff}} (\mu_B)$
370–300	−5.21	−100.08	7.3661	7.67
370–200	−2.27	−33.45	5.14962	6.42
370–100	0.73	24.70	3.40414	5.22
275–100	2.06	34.71	2.96607	4.87
275–100 [7]	3.07	−4		4.82

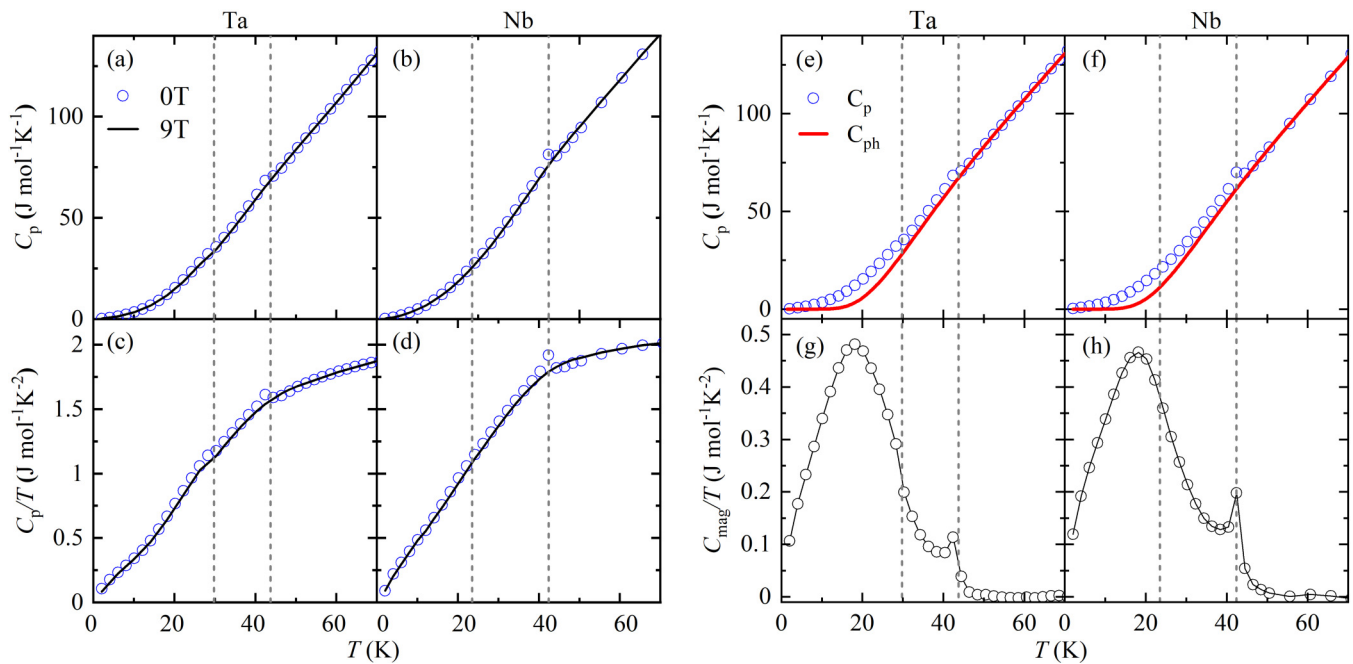


FIG. 4. Heat capacity (C_p) data and analysis. (a), (b) C_p at 0 and 9 T between 2 and 160 K, focusing up to 70 K. (c), (d) Heat capacity divided by temperature, C_p/T . Two lambda-like anomalous temperatures are noted by gray dashed vertical lines in (a)–(d); 43.72 K (42.42 K) for $\text{Ba}_4\text{TaMn}_3\text{O}_{12}$ ($\text{Ba}_4\text{NbMn}_3\text{O}_{12}$) and 29.77 K (23.5 K) for $\text{Ba}_4\text{TaMn}_3\text{O}_{12}$ and ($\text{Ba}_4\text{NbMn}_3\text{O}_{12}$). (e), (f) C_p overplotted with estimated phononic contributions (red lines; see text). (g), (h) Magnetic contribution to heat capacity divided by temperature (C_{mag}/T).

trend in our experiments. θ values from our results are positive in both materials when using the same range of the fitted temperatures.

In Figs. 3(e)–3(h), the magnetization M is plotted against the magnetic field H (between -70 and 70 kOe) with temperatures. At 100 K, the $M(H)$ varies linearly and behaves similarly to a paramagnetic system. The $M(H)$ curves form a hysteresis loop at lower temperatures, compared in Figs. 3(g) and 3(h), where a hysteresis loop in the $M(H)$ data at 2 K disappears at 100 K. This is consistent with the bifurcation anomaly seen in magnetic susceptibility in Figs. 3(a) and 3(b).

D. Heat capacity

We performed heat capacity measurements on the same samples to understand the nature of the anomalous features found in the magnetic susceptibility data. Figures 4(a) and 4(b) present the heat capacity (C_p) of $\text{Ba}_4\text{TaMn}_3\text{O}_{12}$ and $\text{Ba}_4\text{NbMn}_3\text{O}_{12}$, measured between 160 and 2 K at 0 and 9 T. The normalized heat capacity measurements (C_p/T) of $\text{Ba}_4\text{TaMn}_3\text{O}_{12}$ and $\text{Ba}_4\text{NbMn}_3\text{O}_{12}$ are shown in Figs. 4(c) and 4(d) as a function of temperature. Small lambda-like anomalies are observed at around T_1 for both $\text{Ba}_4\text{TaMn}_3\text{O}_{12}$ and $\text{Ba}_4\text{NbMn}_3\text{O}_{12}$ at 0 T. As the temperature was lowered further, heat capacity exhibited additional anomalies at $T_2 \sim 29.77$ K for $\text{Ba}_4\text{TaMn}_3\text{O}_{12}$ and $T_2 \sim 23.5$ K for $\text{Ba}_4\text{NbMn}_3\text{O}_{12}$. Both anomalies at T_1 and T_2 were also seen in $d(\chi T)/dT$ (Fig. 6). In the heat capacity data at 9 T, both anomalies are suppressed, indicating their magnetic origins.

Heat capacity data of magnetic insulators typically consist of a phononic (C_{ph}) and magnetic part (C_{mag}). A normal way

to separate these parts is to subtract the heat capacity data of a nonmagnetic compound having the same crystal structure. However, in the absence of such a nonmagnetic analog, we fitted our heat capacity data with the Debye-Einstein model [23–25], a phenomenological approach to capture the primary characteristic of the complex lattice dynamics. To estimate the lattice contribution, we used a combined model with one Debye term and two Einstein terms, as given by

$$C_{\text{ph}}(T) = f_D C_D(\theta_D, T) + \sum_{i=1}^2 g_i C_{E_i}(\theta_{E_i}, T). \quad (1)$$

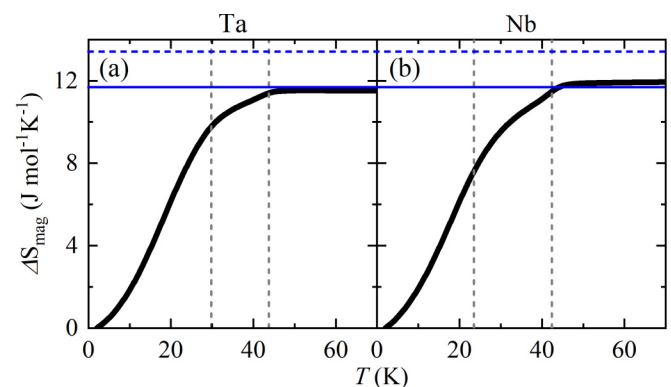


FIG. 5. Evolution of the magnetic entropy [$\Delta S_{\text{mag}}(T)$] of (a) $\text{Ba}_4\text{TaMn}_3\text{O}_{12}$ and (b) $\text{Ba}_4\text{NbMn}_3\text{O}_{12}$. The blue horizontal solid (dashed) lines present the expected entropy for the $S = 3/2$ ($S = 2$) trimer (see text).

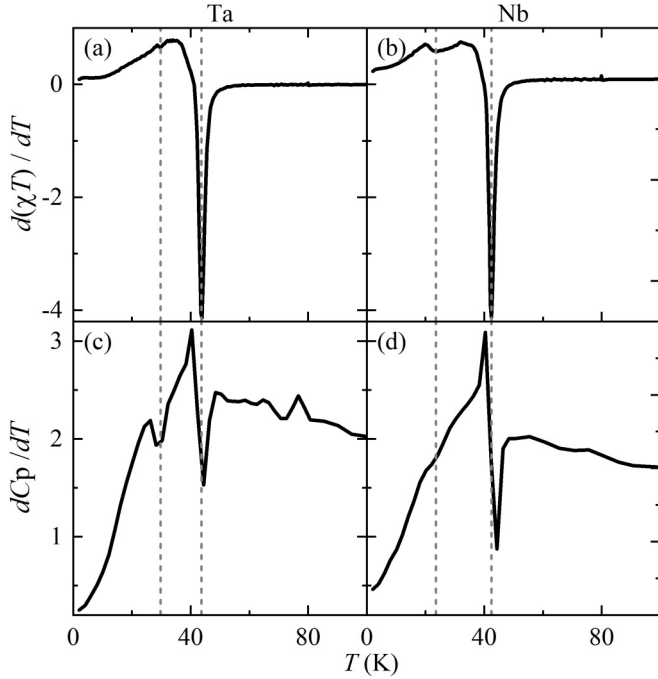


FIG. 6. Comparison of anomalous temperatures from (a), (b) $d(\chi T)/dT$ and (c), (d) dC_p/dT marked by gray dashed vertical lines. $T_1 \sim 43.72$ K and $T_2 \sim 29.77$ K from $\text{Ba}_4\text{TaMn}_3\text{O}_{12}$ and $T_1 \sim 42.42$ K and $T_2 \sim 23.5$ K from $\text{Ba}_4\text{NbMn}_3\text{O}_{12}$.

The first term in Eq. (1) is the Debye term (responsible for the acoustic modes), which is given by

$$C_D(\theta_D, T) = 9nR \left(\frac{T}{\theta_D} \right)^3 \int_0^{\theta_D/T} \frac{x^4 e^x}{(e^x - 1)^2} dx, \quad (2)$$

where n is the number of moles, R is the universal gas constant, θ_D is the characteristic Debye temperature, and $x = \frac{\hbar\omega}{k_B T}$, where ω is the vibrational frequency. The second term contains two Einstein terms (optical modes) and is expressed as

$$C_{E_i}(\theta_{E_i}, T) = 3nR \left(\frac{\theta_{E_i}}{T} \right)^2 \frac{e^{\theta_{E_i}/T}}{(e^{\theta_{E_i}/T} - 1)^2}, \quad (3)$$

where θ_{E_i} is the characteristic Einstein temperature. Since one formula unit of $\text{Ba}_4\mathcal{M}\text{Mn}_3\text{O}_{12}$ consists of 20 atoms, the summed number of f_D and g_i in Eq. (1) is 20, which follows Debye and Einstein statistics, respectively. The heat capacity data, $C_p(T)$, between 50 and 150 K are fitted well with Eq. (1) and the obtained parameters were $f_D \simeq 6$, $g_1 \simeq 8$, $g_2 \simeq 6$, $\theta_D \simeq 1016$ (710) K, $\theta_{E_1} \simeq 404$ (285) K, and $\theta_{E_2} \simeq 145$ (110) K for $\text{Ba}_4\text{TaMn}_3\text{O}_{12}$ ($\text{Ba}_4\text{NbMn}_3\text{O}_{12}$) [red solid lines in Figs. 4(e) and 4(f)]. We also tested the fit using a Debye term and a Debye plus Einstein term, but the fits did not work. Thus we used a Debye term and two Einstein terms as a minimal set of terms in the representative fit in this work. We estimated the magnetic contribution to heat capacity (C_{mag}) by subtracting the phonon contribution (C_{ph}) from the measured heat capacity (C_p) and we extrapolated the fitted curve for temperatures between 160 and 2 K [see solid red lines in Figs. 4(e) and 4(f)]. Figures 4(g) and 4(h) show the values of C_{mag}/T between 2 and 70 K, which reveal a sharp peak

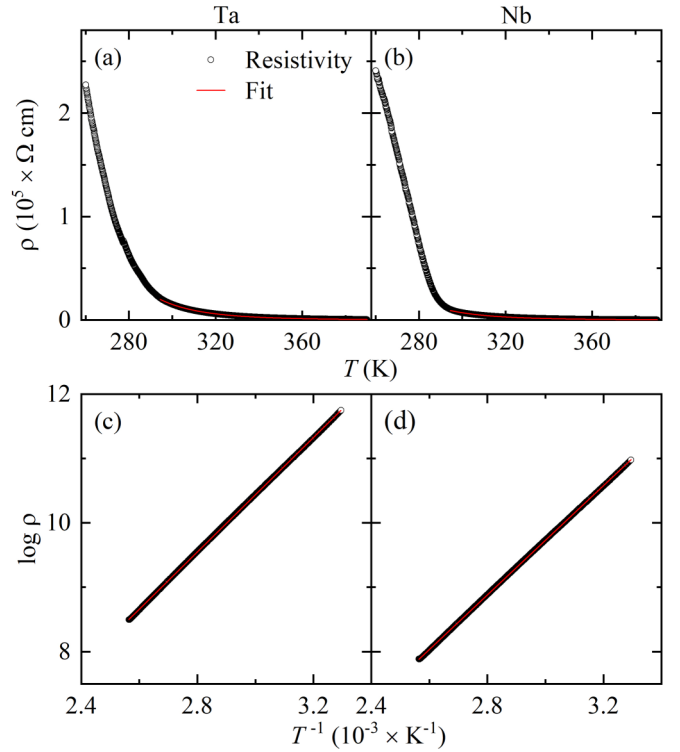


FIG. 7. (a), (b) Resistivity, ρ (Ω cm), versus temperature and (c), (d) $\log \rho$ versus T^{-1} (K^{-1}) of $\text{Ba}_4\text{TaMn}_3\text{O}_{12}$ and $\text{Ba}_4\text{NbMn}_3\text{O}_{12}$, respectively, measured on sintered rectangular pellets. Red solid lines represent the fitted curves (see text).

around T_1 and a broad hump centered at approximately 20 K in both compounds, capturing the magnetic contribution. Note that the number of moles (n) in Eqs. (2) and (3) was not used in our fits.

Figure 5 exhibits the evolution of the magnetic entropy (ΔS_{mag}) between 2 and 70 K. The change in magnetic entropy was calculated by integrating C_{mag}/T with respect to temperature between 2 and 70 K, which yielded the saturated value of $\Delta S_{\text{mag}} = 11.52$ $\text{J mol}^{-1}\text{K}^{-1}$ for $\text{Ba}_4\text{TaMn}_3\text{O}_{12}$ and $\Delta S_{\text{mag}} = 11.94$ $\text{J mol}^{-1}\text{K}^{-1}$ for $\text{Ba}_4\text{NbMn}_3\text{O}_{12}$. Both values are smaller than the expected entropy for the $S = 2$ magnet (dashed horizontal lines in Fig. 5), $\Delta S_{\text{mag}} = R \ln(5) \sim 13.38$ $\text{J mol}^{-1}\text{K}^{-1}$, where R is the gas constant. However, these values are nearly the same as that of the unexpected $S = 3/2$ antiferromagnetic trimer (horizontal solid lines in Fig. 5), $\Delta S_{\text{mag}} = R \ln(4) \sim 11.53$ $\text{J mol}^{-1}\text{K}^{-1}$. Thus our heat capacity analysis suggests the $S = 3/2$ trimer in both compounds, which could not be determined in a previous report [7]. With the uncertainty of the empirically estimated phonons, the agreement of the saturated moments with the expected one for the $S = 3/2$ trimer is satisfactory. The reduced magnetic entropy from that of the $S = 2$ trimer to the $S = 3/2$ trimer can be interpreted by one delocalized electron within the trimer in a partial molecular orbital state (to be explained in Sec. V).

To determine the anomalous temperature more systematically, we compared $d(\chi T)/dT$ and dC_p/dT , finding that the extracted anomalous temperatures (gray dashed vertical lines) from both measurements agreed very well, as shown in Fig. 6. The additional anomaly (T_2) in the magnetic system

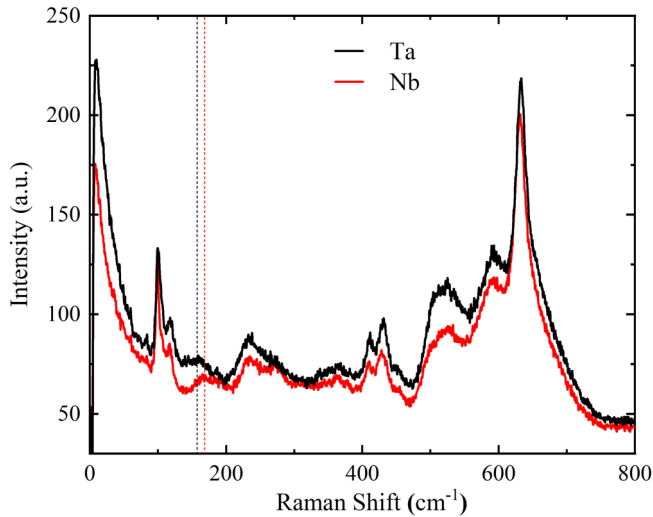


FIG. 8. Comparison of Raman spectra measured at room temperature.

could appear for various reasons, such as an additional magnetic transition, or a (continuous) spin reorientation [27]. It is also possible that a spin-glass transition [28] from a finite disorder occurs at T_1 , followed by the long-range magnetic order at T_2 . Their origins can be examined via other complementary measurements, such as neutron diffraction, in future studies.

E. Resistivity

Figure 7 shows the resistivity data of $\text{Ba}_4\text{TaMn}_3\text{O}_{12}$ and $\text{Ba}_4\text{NbMn}_3\text{O}_{12}$ between 260 and 390 K. Data below 260 K were not obtained due to the exceedingly large resistivity that prevented any measurements in that region in our resistivity option of PPMS. Consequently, we fitted the data between 300 and 390 K with the resistivity equation $\rho = \rho_0 e^{\frac{E_a}{k_B T}}$ to obtain activation energy of transport, E_a , which was found to be 0.383 eV for $\text{Ba}_4\text{TaMn}_3\text{O}_{12}$ and $E_a = 0.365$ eV for $\text{Ba}_4\text{NbMn}_3\text{O}_{12}$. Thus it was confirmed that both materials exhibited semiconductor properties.

F. Raman scattering

Raman spectroscopy is a suitable technique for examining phonons sensitive to crystal structural variations. We performed Raman measurements on both compounds at room temperature to confirm the sample quality and explore lattice dynamics. Figure 8 compares similar phonons of two compounds. Although we included measurements up to 1100 cm^{-1} , multiple phonon peaks are merely observed beyond 800 cm^{-1} . The sharp phonon peaks observed indicate the good qualities of our polycrystalline samples. A phonon of $\text{Ba}_4\text{TaMn}_3\text{O}_{12}$ at approximately 180 cm^{-1} is slightly softened, possibly because Ta ions are heavier than Nb ions. In contrast, Raman phonon spectra at higher energies are more similar, which could be explained by the lighter ions Mn and O. Raman measurements at lower temperatures (i.e., lower than the anomalous temperatures obtained from susceptibility and heat capacity measurements) might be sensitive in detecting bond angle changes and distances in the magnetically

ordered state by spin-lattice coupling [29]. These measurements may also provide information on magnetic ground states and exchange interaction with respect to molecular orbital states [5].

V. AB INITIO CALCULATIONS

To understand the electronic structure and magnetism of both compounds, we performed *ab initio* density functional theory (DFT) calculations. We initially assessed the magnetic nature of the Mn trimer and Fig. 9(a) shows its two simplest magnetic configurations—a ferromagnetic and a ferrimagnetic order in the primitive unit cell. Note that the ferrimagnetic order in this section means the ferrimagnetic trimer in the primitive unit cell. We found that the total energy per formula unit of the ferrimagnetic order was lower than that of the ferromagnetic case for $\text{Ba}_4\text{NbMn}_3\text{O}_{12}$ and $\text{Ba}_4\text{TaMn}_3\text{O}_{12}$ by 62.7 meV and 55.9 meV, respectively. This could be attributed to the antiferromagnetic coupling between Mn-Mn in the face-sharing MnO_6 octahedra originating from a strong direct orbital overlap between Mn 3d orbitals discussed in previous literature [15].

On the one hand, a molecular orbital (MO) state is proposed in a 4d [4] and 5d [5] transition-metal compound with a similar crystal structure (the trimer with the face-sharing octahedra) owing to the strong direct overlap of orbitals. On the other hand, we identified that the direct overlap between the face-sharing Mn a_{1g} orbitals was significant but not strong enough to break the local moment scheme in both compounds. For instance, Fig. 9(b) presents the projected density of states (PDOS) of $\text{Ba}_4\text{NbMn}_3\text{O}_{12}$ (a top panel) and $\text{Ba}_4\text{TaMn}_3\text{O}_{12}$ (a bottom panel) in the ferrimagnetic configuration, where the atomic exchange splitting due to Hund's coupling is larger than the energy splitting induced by the direct orbital overlap in the face-sharing geometry. Hence the t_{2g} shell was half filled with a robust $S = 3/2$ local moment at each Mn site in the antiferromagnetic trimer. In Fig. 9(b), this is evident from six electrons occupying the t_{2g} down-spin orbital and three electrons occupying the t_{2g} up-spin orbitals.

Interestingly, unlike the t_{2g} shell, one electron having the e_g character in an Mn^{3+} ion was strikingly delocalized and preferred a metallic phase in the ferrimagnetic state. The e_g orbital at the central Mn site was almost empty, whereas one electron is equally shared by the e_g orbitals at the top and bottom Mn site, as illustrated in Fig. 9(b). This is reminiscent of a similar 4d analog for $\text{Ba}_4\text{Ru}_3\text{O}_{10}$ [3,4], where the middle ion of the Ru trimer was nonmagnetic. Hence the total spin moment at the Mn trimer became $S = 2$, which is decomposed into the localized t_{2g} ($S = 3/2$) and delocalized e_g ($S = 1/2$) components. Note that this observation is also consistent with our magnetic susceptibility (Fig. 3) and heat capacity data (Fig. 5).

Figure 9(c) shows the calculated band structure, revealing that the partially filled e_g band (solid blue lines) exhibits a strong two-dimensional character of an almost flat dispersion along with the Z - Γ line parallel to the Mn trimer along the c axis. In contrast, our resistivity data in Fig. 7 strongly suggest that both $\text{Ba}_4\text{NbMn}_3\text{O}_{12}$ and $\text{Ba}_4\text{TaMn}_3\text{O}_{12}$ are gapped. This is due to a well known flaw of the DFT method, which cannot capture the paramagnetic Mott phase as it cannot describe

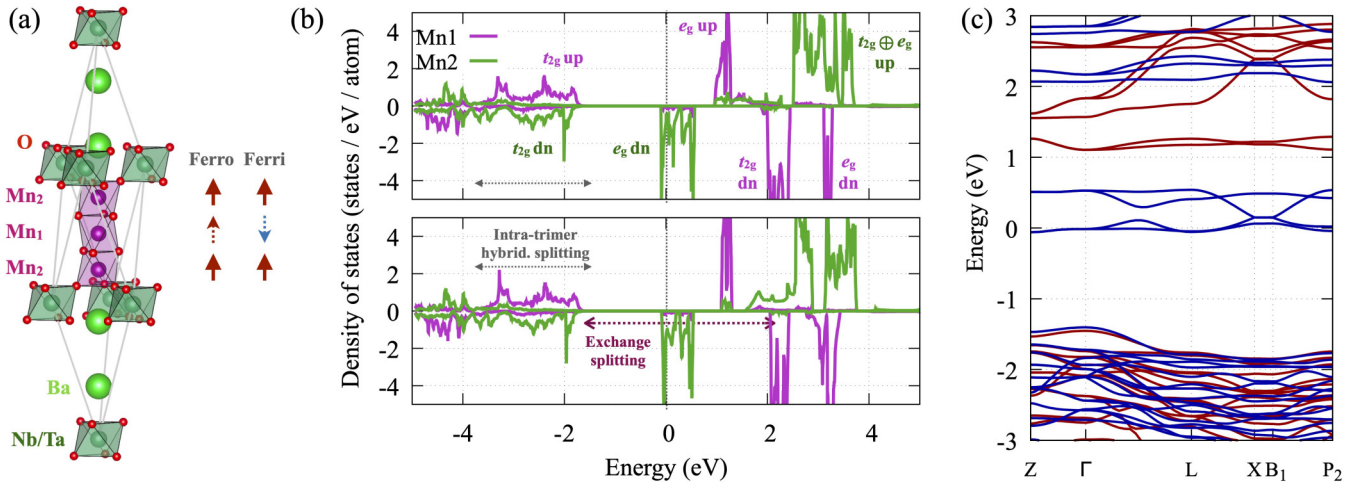


FIG. 9. (a) Primitive rhombohedral unit cell of $\text{Ba}_4\text{NbMn}_3\text{O}_{12}$ and $\text{Ba}_4\text{TaMn}_3\text{O}_{12}$, where the two simplest magnetic configurations at Mn trimer are shown on the right. Note that Mn atoms at the center and two sides of the Mn trimer are denoted as Mn_1 and Mn_2 , respectively (consistent with Tables I and II). $S = 3/2$ moments at Mn_1 sites are depicted as dotted arrows. (b) Projected density of states (PDOS) for $\text{Ba}_4\text{NbMn}_3\text{O}_{12}$ (a top panel) and $\text{Ba}_4\text{TaMn}_3\text{O}_{12}$ (a bottom panel), where the energy splitting by hybridization and exchange energy is shown. (c) Band structure of $\text{Ba}_4\text{TaMn}_3\text{O}_{12}$ with the ferrimagnetic trimer in the primitive unit cell shown in (a). Red and blue lines depict spin-up and -down bands, respectively. Note that the band of $\text{Ba}_4\text{NbMn}_3\text{O}_{12}$ is qualitatively the same as that of $\text{Ba}_4\text{TaMn}_3\text{O}_{12}$ (not shown). Conventions for high-symmetry points follow the ones described in Ref. [26].

fluctuating magnetic moments. However, the magnetic fluctuation diminishes in the long-range magnetic order below the transition temperature, where the DFT method can provide a qualitatively valid picture. The nature of the band gap can be examined via dynamical mean-field theory calculations in further study, by properly considering fluctuating magnetic moments.

To determine a possible magnetic ground state, we used the two simplest antiferromagnetic configurations (denoted as AF1 and AF2) by adopting the ferrimagnetic Mn trimer as the magnetic building block [see Figs. 10(a) and 10(b)]. The AF1 state contains a magnetic unit cell that is twice enlarged along the c axis compared to the parent nuclear unit cell with a wave vector, $q = (0, 0, 1/2)$, whereas the AF2 state has a doubled unit cell along the a axis in an orthorhombic magnetic unit cell based on the in-plane antiferromagnetic order, $q = (1/2, 0, 0)$. We set up the AF1 state based on information provided in Ref. [15], where the antiferromagnetic order within the trimer is coupled ferromagnetically in the ab plane and antiferromagnetically along the c axis. In our calculations, we detected that the total energy of the orthorhombic AF2 configuration is lower by 178.9 meV and 85.0 meV per formula unit than that of the AF1 state for $\text{Ba}_4\text{NbMn}_3\text{O}_{12}$ and $\text{Ba}_4\text{TaMn}_3\text{O}_{12}$, respectively. We also found a similar tendency of the MO state in both compounds. Note that our calculated band gap of $\text{Ba}_4\text{TaMn}_3\text{O}_{12}$ is vanishingly small even in the orthorhombic configuration with $U_{\text{eff}} = 4$ eV for both compounds. We point out that the AF2 state is a collinear antiferromagnetic order, which can serve as a good approximate magnetic structure.

VI. DISCUSSION

We are in a position to discuss the nature of the Mn trimer in $\text{Ba}_4\mathcal{M}\text{Mn}_3\text{O}_{12}$ ($\mathcal{M} = \text{Ta}, \text{Nb}$). Our first-principle

calculations predict an unusual combination of localized and delocalized electrons; that is, the localized antiferromagnetic magnetic moments ($S = 3/2$) within the trimer and one electron delocalized in the two-end Mn ions of the trimer. Our picture can be compatible with both magnetic susceptibility (Sec. IV C) and heat capacity results (Sec. IV D).

In magnetic susceptibility experiments, we found that the effective magnetic moments from a paramagnetic temperature indicate the $S = 2$ trimer in both compounds. They are compatible with the effective magnetic moments reported in Ref. [7] for $\text{Ba}_4\text{NbMn}_3\text{O}_{12}$. At first, our results might be counterintuitive because of the localized $S = 3/2$ trimer in $\text{Ba}_4\mathcal{M}\text{Mn}_3\text{O}_{12}$. However, they can be explained by the additional contribution from one delocalized electron in the trimer. For instance, the effective magnetic moments above the transition temperature reported in weakly ferromagnetic itinerant metals, such as ZrZn_2 [30] and Sc_3In [30], are much bigger than those expected from the small ordered magnetic moment; i.e., in ZrZn_2 , the saturated magnetic moment is only about $0.12 \mu\text{B}$ [30,31], whereas the effective magnetic moment obtained from the Curie-Weiss-like law is about $1.4 \mu\text{B}$ [31,32], close to the effective magnetic moment of spin-1/2, $1.73 \mu\text{B}$. These experimental observations are understood by the interaction of spatially extended modes of spin fluctuations, giving the Curie-Weiss-like behavior with a large effective magnetic moment [30,31,33]. Since the experimental observations in itinerant magnetic systems are consistent with our observations, a similar microscopic mechanism could be applied to the delocalized electron in $\text{Ba}_4\mathcal{M}\text{Mn}_3\text{O}_{12}$.

Possible origins of the weak hysteresis in the magnetization data could be associated with various reasons, such as the ferrimagnetic moments deviating from the collinear antiferromagnetic moments and a spin glass feature from the finite disorder. Further magnetic susceptibility measurements could reveal the nature of the magnetic ground state.

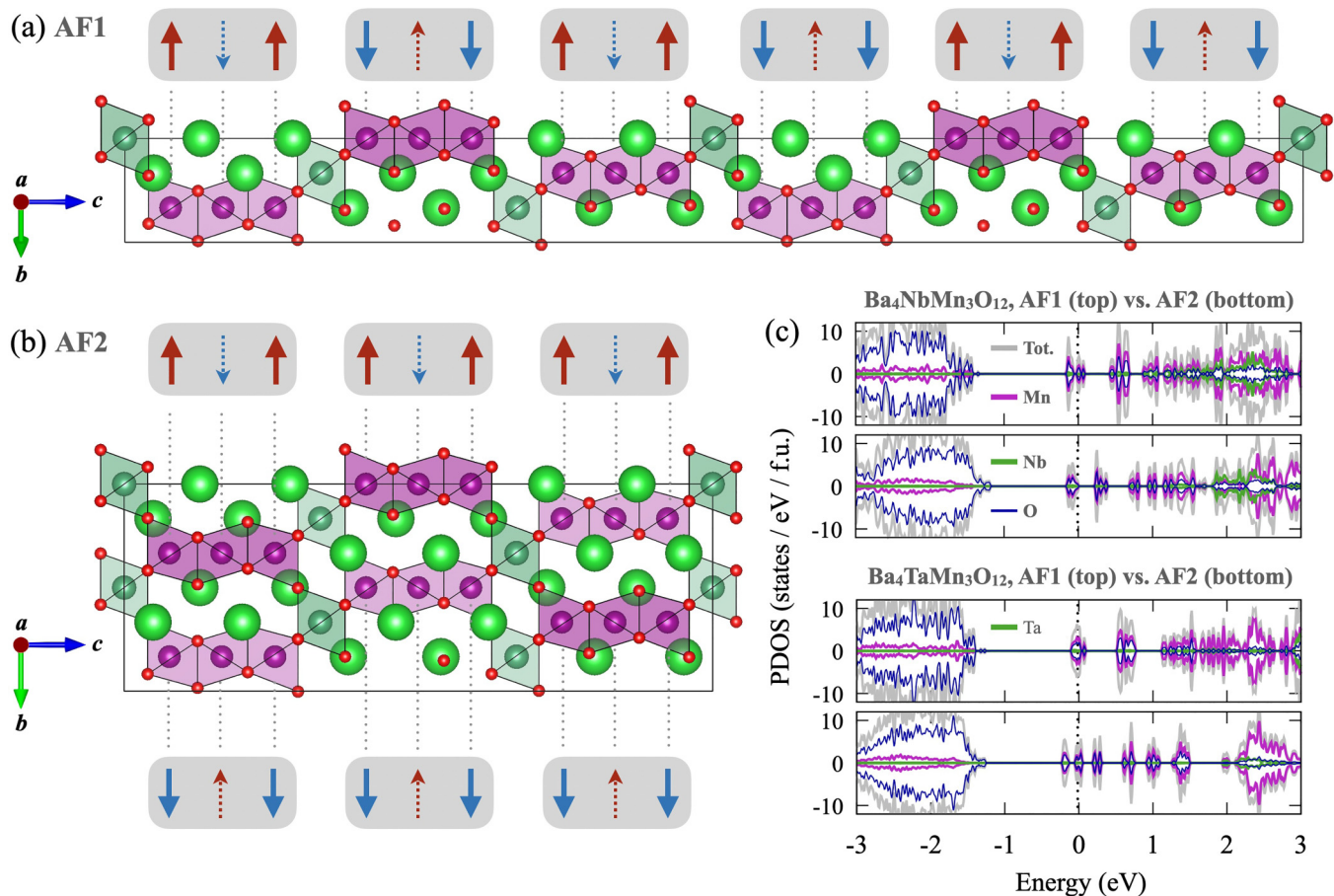


FIG. 10. Results of band structure calculations of the two simplest antiferromagnetic magnetic configurations. (a) AF1 and (b) AF2, which employ the Mn trimer as a magnetic unit. (c) PDOS for $\text{Ba}_4\text{NbMn}_3\text{O}_{12}$ (upper panels) and $\text{Ba}_4\text{TaMn}_3\text{O}_{12}$ (lower panels), where the top and bottom ones correspond to PDOS of the AF1 and AF2 configuration, respectively.

For instance, such states could be studied via ac magnetic susceptibility measurements, by probing domain walls of ferromagnetic order, or by confirming freezing temperatures with the shift of the ac data by different oscillating frequencies [34]. These measurements will reveal the existence of finite disorder, which might result in the weak hysteric behavior in the magnetization data [Figs. 3(g) and 3(h)].

In addition, we checked the possible existence of the “unpaired” $S = 2$ moment in both compounds using the susceptibility data [Figs. 3(a) and 3(b)]. If one e_g electron is localized in one of the two-end Mn ions of the trimer without forming a partial molecular orbital, the fully localized $S = 2$ moment will be possible in the sample. Since the unpaired $S = 2$ will not have a presumed long-ranged spin-spin correlation with other normal trimers, we tabulated it with the paramagnetic term of C_u/T in the revised Curie-Weiss fit, where C_u means the Curie constant of the unpaired moment. The revised fits did not work and gave diverging results, meaning no significant fraction of the impurity state. This outcome is consistent with our additional DFT + U_{eff} calculations (not shown), which confirm that such a state is unstable in the realistic range of U_{eff} ($3 < U_{\text{eff}} < 5$ eV). Instead, we found that all initial configurations that started with the unpaired state converged to the partial molecular orbital state in our calculations.

In heat capacity measurements, we clearly showed that the magnetic entropy between 2 and 70 K is only $S = 3/2$, not $S = 2$ (Fig. 5) in both compounds. One might suggest that the reduction of the magnetic entropy in Fig. 5 is led by the strong quantum fluctuations due to the frustrated magnetic exchanges [35]. However, this seems less likely as the frustration indexes ($f = |\theta|/T_1$) [36] are tiny in both compounds, although we cannot completely rule out a possibility of a sizable magnetic entropy below 2 K. Note that highly frustrated magnetic materials usually reveal a large frustration factor, f [37].

As a more feasible explanation, we point out that the magnetic entropy of the itinerant magnet [38] is much smaller than that of the localized magnets. A tiny fraction of the magnetic entropy can be released via the magnetic transition in the itinerant magnet; for instance, only 2% of the $S = 1/2$ magnetic entropy ($\Delta S_{\text{mag}} = 0.02R \ln 2$) was reported for the weakly ferromagnetic metal ZrZn_2 [38,39]. Hence it will be sensible to interpret that our heat capacity measurements detect the magnetic entropy dominantly released by the long-range magnetic order from the localized magnetic moment in both compounds. We note that Ref. [7] reported a puzzling magnetic entropy of $\text{Ba}_4\text{NbMn}_3\text{O}_{12}$, which is much smaller than the values expected for both the $S = 2$ and $S = 3/2$ trimer. In our heat capacity measurements, we resolved this issue by using optimally grown polycrystalline samples.

Based on our results on $\text{Ba}_4\mathcal{M}\text{Mn}_3\text{O}_{12}$ ($\mathcal{M} = \text{Ta}, \text{Nb}$) presented in this paper, further investigation of these peculiar magnetic properties would be highly desired. Pertaining to $\text{Ba}_4\text{NbMn}_3\text{O}_{12}$, Ref. [7] suggested the presence of ordered magnetic moments inside the trimer even at 300 K; however, the long-range magnetic order stabilized by the intertrimer exchange interactions appeared only at a lower temperature [7]. Thus neutron diffraction as a bulk probe will be useful to determine the magnetic structure and its evolution with temperature, which are related to the magnetic anomalies found in susceptibility measurements (Fig. 3). On the other hand, muon spin relaxation as a local probe can measure the local magnetic field sensitively; for instance, it is suitable for studying static and dynamic magnetic properties of $\text{Ba}_4\mathcal{M}\text{Mn}_3\text{O}_{12}$ ($\mathcal{M} = \text{Ta}, \text{Nb}$). Thus the nature of the unusual paramagnetic state and the coexistence of localized and delocalized magnetism might be investigated by muons. These measurements could be sensitive to confirm the $S = 3/2$ trimer in the localized moment picture.

Moreover, the underlying spin Hamiltonian for these compounds needs to be studied experimentally. In these compounds, spin dynamics can be determined by the inter- and intratrimer interaction of the Mn_3O_{12} trimer because only Mn ions are magnetic (i.e., nonmagnetic Ba^{2+} and Nb^{5+} ions). A recent theory [15] suggested a ferromagnetic exchange in the ab plane that is antiferromagnetically coupled along the c axis. Consequently, inelastic neutron scattering (INS) will be crucial to assess the number of effectively dominant exchange couplings and their characteristics by testing various models, including the proposed one. As we found a strong coupling between Mn spins within the trimer from extracted effective moments at high temperatures [CW fits in Figs. 3(c) and 3(d)], high-energy magnetic signals excited within the trimer are expected in INS measurements; for example, strong antiferromagnetic interactions between the middle and end Mn ions are anticipated in the AF2 model [Fig. 10(b)]. Thus INS could be suitable to probe the $S = 3/2$ trimer based on the energy and intensity of the trimer excitation.

Unlike the more studied $4d$ and $5d$ trimer-based materials [21,22,40], our results on $\text{Ba}_4\mathcal{M}\text{Mn}_3\text{O}_{12}$ ($\mathcal{M} = \text{Ta}, \text{Nb}$) suggest an unconventional character—a partial molecular orbital state. Figure 11 visualizes the wave functions of the partial molecular orbital state at the Γ point of $\text{Ba}_4\text{TaMn}_3\text{O}_{12}$ [Fig. 9(b)], demonstrating the absence of the e_g electron in the central Mn ion. Also, it confirms that the electrons are not delocalized across the trimers via Ta/Nb d orbitals. It is microscopically because the Ta/Nb orbitals are located at much higher energies, which makes the overlap ineffective [Fig. 9(b)].

The crucial difference for the different electronic structures of the $3d$ and $4d/5d$ compounds comes from the distinct hierarchy of the microscopic energy scales. In the $3d$ case for $\text{Ba}_4\mathcal{M}\text{Mn}_3\text{O}_{12}$, the Coulomb interaction (U) is dominant. It is stronger than the intersite hybridization energy within the Mn trimer and the exchange splitting (Hund's coupling) [Fig. 9(b)], which stabilizes the dominant local moment. This is a strongly localized scheme. The signs of p -orbital lobes surrounding the central Mn (in the overlap of ligand p orbitals) are inversion antisymmetric for all four partial molecular orbital wave functions, effectively

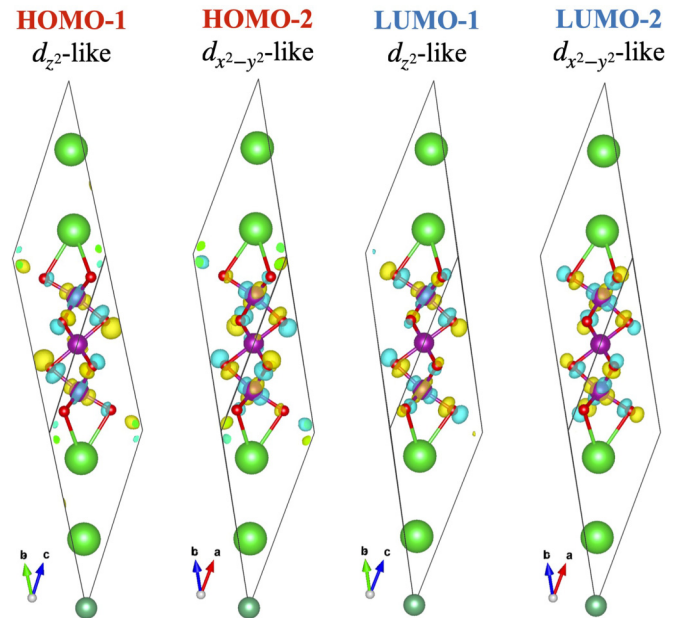


FIG. 11. HOMO (highest energy occupied molecular orbital) and LUMO (lowest energy unoccupied molecular orbital) wave functions of $\text{Ba}_4\text{TaMn}_3\text{O}_{12}$ at the Γ point in Fig. 9(b). Violet and red spheres are Mn and O ions, respectively. Ta ions are not shown as there is practically no contribution in the wave functions.

canceling inversion-symmetric d -orbital components at the central Mn ion. On the other hand, in the $4d/5d$ counterparts $\text{Ba}_4\text{Nb}\mathcal{M}_3\text{O}_{12}$ ($\mathcal{M} = \text{Ru}, \text{Ir}$), the intersite hybridization energy is dominant, stabilizing the molecular orbital state [21].

This noteworthy difference in their natures of MO states implies a further research opportunity to examine the crossover between atomic and molecular descriptions of magnetism by mixing $3d$ ions with heavier $4d$ or $5d$ ions; in particular, $\text{Ba}_4\text{NbRu}_3\text{O}_{12}$ [21] and $\text{Ba}_4\text{NbIr}_3\text{O}_{12}$ [40] can be synthesized. We note that the electronic structure and magnetism of $\text{Ba}_4\mathcal{M}\text{Mn}_3\text{O}_{12}$ resemble those of the metallic double exchange in $\text{La}_x\text{Sr}_{1-x}\text{MnO}_3$ [41,42], indicating that a possible ferromagnetic metallic phase in $\text{Ba}_4\mathcal{M}\text{Mn}_3\text{O}_{12}$ might be realized via an external magnetic field, pressure, or doping, which can be potentially useful in spintronics and magnetic devices.

Finally, in addition to $\text{Ba}_4\mathcal{M}\text{Mn}_3\text{O}_{12}$ ($\mathcal{M} = \text{Ta}, \text{Nb}$), a wide range of different compositions is possible in the similar hexagonal perovskite, $\text{Ba}_4\mathcal{M}\mathcal{M}'_3\text{O}_{12}$ ($\mathcal{M} = \text{Nb}, \text{Ta}, \text{Ce}, \text{Pr}$ and $\mathcal{M}' = \text{Mn}, \text{Ru}, \text{Ir}$) [21,43–46] with face-sharing trimer octahedra. Therefore, this compound family is versatile but a less-studied platform for searching for unconventional magnetic properties, including molecular orbital-based magnetism [47,48], calling for both experimental and theoretical studies in the future.

VII. CONCLUSIONS

We reported an unconventional molecular orbital candidate $\text{Ba}_4\text{TaMn}_3\text{O}_{12}$ by comparing it to a recently reported compound $\text{Ba}_4\text{NbMn}_3\text{O}_{12}$. We synthesized the polycrystalline sample by optimizing the amount of the MnO_2 starting

powder monitored by x-ray diffraction measurements. Both magnetic susceptibility and heat capacity measurements revealed two compatible anomalies. Susceptibility showed the dominance of ferromagnetic intertrimer interaction. The effective magnetic moments indicated the strong coupling between spins within the trimer above the magnetic ordering temperature. The estimated magnetic entropy from heat capacity measurements is consistent with the antiferromagnetic $S = 3/2$ trimer with localized moments. These results indicate the combination of the localized $S = 3/2$ and one delocalized electron in the trimer. *Ab initio* calculations found that three localized electrons are present in each of the three Mn ions and one delocalized electron is spread over two-end Mn ions of the trimer, consistent with both susceptibility and heat capacity results. The magnetic ordering wave vector is predicted to be $q = (1/2, 0, 0)$. Thus our comprehensive results propose the partial molecular orbital in 3d trimer-based materials—an unconventional electronic state with delocalized and localized electrons in a single compound. This could be understood by the competition between the hybrid interatomic orbitals within the Mn trimer and the local moment formation by on-site Coulomb correlations. In searching for novel electronic states, the possibility of finding the insulator-metal transition in this compound family by an external magnetic field, pressure, or doping warrants active further investigations in the future.

ACKNOWLEDGMENTS

This work was supported by the Institute for Basic Science (Grant No. IBS-R011-Y3) and Advanced Facility Center for Quantum Technology at Sungkyunkwan University. Part of this study has been performed using facilities at IBS Center for Correlated Electron Systems, Seoul National University. H.-S.K. acknowledges the support of the National Research Foundation of Korea (Basic Science Research Program, Grant No. 2020R1C1C1005900, RS-2023-00220471) and the support of computational resources, including technical assistance from the National Supercomputing Center of Korea (Grant No. KSC-2022-CRE-0358).

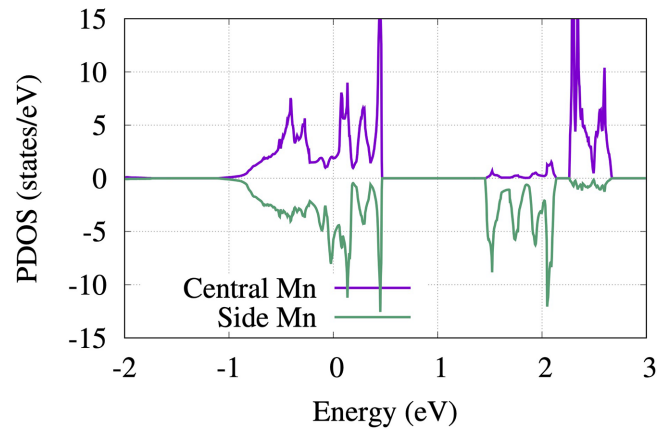


FIG. 12. Projected densities of states for central and side Mn atoms within the Mn trimer from nonmagnetic DFT calculations without U_{eff} . Note that t_{2g} orbital states are close to the Fermi level ($E = 0$) and e_g orbital states are located between 1.5 and 3 eV.

APPENDIX: NONMAGNETIC DFT CALCULATIONS

To understand the physics above the magnetic transition temperature, we performed additional DFT calculations. Figure 12 shows Mn-site-projected densities of states from a nonmagnetic DFT calculation without U_{eff} . Therein it can be seen that the t_{2g} - e_g splitting in central and side Mn sites are about 2.5 and 1.8 eV, respectively, whereas the strength of intersite hybridization within the Mn trimer (\sim the bandwidth of t_{2g} and e_g orbitals) is shown to be about 1 eV. We note that Fig. 9(b) presents that the size of the exchange splitting is about 4 eV when $U_{\text{eff}} = 4$ eV in our DFT + U_{eff} calculations. A separate calculation employing a parameter-free r2SCAN meta-GGA functional [49] reveals the size of the exchange splitting to be about 4 eV, which is consistent with results in Fig. 9(b). Overall, the hierarchy of on-site energy scales at Mn sites is as follows: Coulomb interaction (U) > exchange splitting (Hund's coupling) > cubic crystal fields (t_{2g} - e_g splitting) > intersite hybridization within Mn trimer. This relation stabilizes the partial molecular orbital state in $\text{Ba}_4\mathcal{M}\text{Mn}_3\text{O}_{12}$ ($\mathcal{M} = \text{Ta}, \text{Nb}$).

- [1] M. Imada, A. Fujimori, and Y. Tokura, Metal-insulator transitions, *Rev. Mod. Phys.* **70**, 1039 (1998).
- [2] S. V. Streltsov and D. I. Khomskii, Orbital physics in transition metal compounds: new trends, *Phys.-Uspekhi* **60**, 1121 (2017).
- [3] Y. Klein, G. Rousse, F. Damay, F. Porcher, G. André, and I. Terasaki, Antiferromagnetic order and consequences on the transport properties of $\text{Ba}_4\text{Ru}_3\text{O}_{10}$, *Phys. Rev. B* **84**, 054439 (2011).
- [4] S. V. Streltsov and D. I. Khomskii, Unconventional magnetism as a consequence of the charge disproportionation and the molecular orbital formation in $\text{Ba}_4\text{Ru}_3\text{O}_{10}$, *Phys. Rev. B* **86**, 064429 (2012).
- [5] M. Ye, H.-S. Kim, J.-W. Kim, C.-J. Won, K. Haule, D. Vanderbilt, S.-W. Cheong, and G. Blumberg, Covalency-driven collapse of strong spin-orbit coupling in face-sharing iridium octahedra, *Phys. Rev. B* **98**, 201105(R) (2018).
- [6] A. Georges, L. d. Medici, and J. Mravlje, Strong correlations from hund's coupling, *Annu. Rev. Condens. Matter Phys.* **4**, 137 (2013).
- [7] L. T. Nguyen, T. Kong, and R. J. Cava, Trimers of MnO_6 octahedra and ferrimagnetism of $\text{Ba}_4\text{NbMn}_3\text{O}_{12}$, *Mater. Res. Express* **6**, 056108 (2019).
- [8] K. Poeppelmeier, M. Leonowicz, J. Scanlon, J. Longo, and W. Yelon, Structure determination of CaMnO_3 and $\text{CaMnO}_{2.5}$ by X-ray and neutron methods, *J. Solid State Chem.* **45**, 71 (1982).
- [9] The Materials Project, <https://materialsproject.org/materials/mp-8634/>.
- [10] V. Petříček, M. Dušek, and L. Palatinus, Crystallographic computing system Jana2006: General features, *Z. Kristallogr. - Cryst. Mater.* **229**, 345 (2014).
- [11] G. Kresse and J. Hafner, *Ab initio* molecular dynamics for liquid metals, *Phys. Rev. B* **47**, 558 (1993).

- [12] G. Kresse and J. Furthmüller, Efficient iterative schemes for *ab initio* total-energy calculations using a plane-wave basis set, *Phys. Rev. B* **54**, 11169 (1996).
- [13] S. L. Dudarev, G. A. Botton, S. Y. Savrasov, C. J. Humphreys, and A. P. Sutton, Electron-energy-loss spectra and the structural stability of nickel oxide: An LSDA+U study, *Phys. Rev. B* **57**, 1505 (1998).
- [14] A. T. Lee and M. J. Han, Charge transfer, confinement, and ferromagnetism in LaMnO₃/LaNiO₃ (001) superlattices, *Phys. Rev. B* **88**, 035126 (2013).
- [15] S. V. Streltsov and D. I. Khomskii, Cluster magnetism of Ba₄NbMn₃O₁₂: Localized electrons or molecular orbitals? *JETP Lett.* **108**, 686 (2018).
- [16] H.-S. Kim, K. Haule, and D. Vanderbilt, Mott metal-insulator transitions in pressurized layered trichalcogenides, *Phys. Rev. Lett.* **123**, 236401 (2019).
- [17] N. C. Harms, H.-S. Kim, A. J. Clune, K. A. Smith, K. R. O'Neal, A. V. Haglund, D. G. Mandrus, Z. Liu, K. Haule, D. Vanderbilt, and J. L. Musfeldt, Piezochromism in the magnetic chalcogenide MnPS₃, *npj Quantum Mater.* **5**, 56 (2020).
- [18] S. I. Ali, R. K. Kremer, and M. Johnsson, Hydrothermal synthesis and magnetic characterization of the quaternary oxide CoMo₂Sb₂O₁₀, *Inorg. Chem.* **55**, 11490 (2016).
- [19] S. Mugiraneza and A. M. Hallas, Tutorial: a beginner's guide to interpreting magnetic susceptibility data with the Curie-Weiss law, *Commun. Phys.* **5**, 95 (2022).
- [20] R. L. Carlin, *Magnetochemistry* (Springer, Berlin, 1986).
- [21] L. T. Nguyen, T. Halloran, W. Xie, T. Kong, C. L. Broholm, and R. J. Cava, Geometrically frustrated trimer-based mott insulator, *Phys. Rev. Mater.* **2**, 054414 (2018).
- [22] G. S. Thakur, S. Chattopadhyay, T. Doert, T. Herrmannsdörfer, and C. Felser, Crystal growth of spin-frustrated Ba₄Nb_{0.8}Ir_{3.2}O₁₂: A possible spin liquid material, *Cryst. Growth Des.* **20**, 2871 (2020).
- [23] C. Kittel, *Introduction to Solid State Physics*, 8th ed. (John Wiley & Sons, Ltd, New York, 2004).
- [24] K. Caslin, R. K. Kremer, F. S. Razavi, A. Schulz, A. Muñoz, F. Pertlik, J. Liu, M.-H. Whangbo, and J. M. Law, Characterization of the spin- $\frac{1}{2}$ linear-chain ferromagnet CuAs₂O₄, *Phys. Rev. B* **89**, 014412 (2014).
- [25] S. J. Sebastian, K. Somesh, M. Nandi, N. Ahmed, P. Bag, M. Baenitz, B. Koo, J. Sichelschmidt, A. A. Tsirlin, Y. Furukawa, and R. Nath, Quasi-one-dimensional magnetism in the spin- $\frac{1}{2}$ antiferromagnet BaNa₂Cu(VO₄)₂, *Phys. Rev. B* **103**, 064413 (2021).
- [26] W. Setyawan and S. Curtarolo, High-throughput electronic band structure calculations: Challenges and tools, *Comput. Mater. Sci.* **49**, 299 (2010).
- [27] R. L. White, Review of Recent Work on the Magnetic and Spectroscopic Properties of the Rare-Earth Orthoferrites, *J. Appl. Phys.* **40**, 1061 (1969).
- [28] O. Young, L. C. Chapon, and O. A. Petrenko, Low temperature magnetic structure of geometrically frustrated SrHo₂O₄, *J. Phys.: Conf. Ser.* **391**, 012081 (2012).
- [29] L. D. Casto, A. J. Clune, M. O. Yokosuk, J. L. Musfeldt, T. J. Williams, H. L. Zhuang, M.-W. Lin, K. Xiao, R. G. Hennig, B. C. Sales, J.-Q. Yan, and D. Mandrus, Strong spin-lattice coupling in CrSiTe₃, *APL Mater.* **3**, 041515 (2015).
- [30] T. Moriya and Y. Takahashi, Itinerant electron magnetism, *Annu. Rev. Mater. Sci.* **14**, 1 (1984).
- [31] T. Moriya, *Spin Fluctuations in Itinerant Electron Magnetism* (Springer, Heidelberg, 1985).
- [32] É. du T. de Lacheisserie, D. Gignoux, and M. Schlenker, *Magnetism: Fundamentals, Materials and Applications* (Springer, New York, 2002).
- [33] T. Moriya, Theory of itinerant electron magnetism, *J. Magn. Magn. Mater.* **100**, 261 (1991).
- [34] C. V. Topping and S. J. Blundell, A.c. susceptibility as a probe of low-frequency magnetic dynamics, *J. Phys.: Condens. Matter* **31**, 013001 (2019).
- [35] R. Zhong, S. Guo, G. Xu, Z. Xu, and R. J. Cava, Strong quantum fluctuations in a quantum spin liquid candidate with a Co-based triangular lattice, *Proc. Natl. Acad. Sci. USA* **116**, 14505 (2019).
- [36] A. Ramirez, *Handbook of Magnetic Materials* (Gulf Professional Publishing, Houston, TX, 2001), Vol. 13, Chap. 4, p. 423.
- [37] L. Balents, Spin liquids in frustrated magnets, *Nature (London)* **464**, 199 (2010).
- [38] E. P. Wohlfarth, Thermodynamic aspects of itinerant electron magnetism, *Physica B+C* **91**, 305 (1977).
- [39] R. Viswanathan and J. R. Clinton, Magnetic entropy and magnetization of ZrZn₂, *AIP Conf. Proc.* **24**, 416 (1975).
- [40] L. T. Nguyen and R. J. Cava, Trimer-based spin liquid candidate Ba₄NbIr₃O₁₂, *Phys. Rev. Mater.* **3**, 014412 (2019).
- [41] J.-H. Park, E. Vescovo, H.-J. Kim, C. Kwon, R. Ramesh, and T. Venkatesan, Direct evidence for a half-metallic ferromagnet, *Nature (London)* **392**, 794 (1998).
- [42] S. Majumdar and S. van Dijken, Pulsed laser deposition of La_{1-x}Sr_xMnO₃: thin-film properties and spintronic applications, *J. Phys. D: Appl. Phys.* **47**, 034010 (2014).
- [43] A. F. Fuentes, K. Boulahya, and U. Amador, Novel rare-earth-containing manganites Ba₄REMn₃O₁₂ (RE=Ce, Pr) with 12R structure, *J. Solid State Chem.* **177**, 714 (2004).
- [44] Y. Shimoda, Y. Doi, M. Wakeshima, and Y. Hinatsu, Magnetic and electrical properties of quadruple perovskites with 12 layer structures Ba₄LnM₃O₁₂ (Ln=Rare earths; M=Ru, Ir): The role of metal-metal bonding in perovskite-related oxides, *J. Solid State Chem.* **183**, 1962 (2010).
- [45] Y. Shimoda, Y. Doi, Y. Hinatsu, and K. Ohoyama, Synthesis, crystal structures, and magnetic properties of new 12L-perovskites Ba₄LnRu₃O₁₂ (Ln = Lanthanides), *Chem. Mater.* **20**, 4512 (2008).
- [46] Y. Shimoda, Y. Doi, M. Wakeshima, and Y. Hinatsu, Synthesis and magnetic properties of 12L-perovskites Ba₄LnIr₃O₁₂ (Ln=Lanthanides), *J. Solid State Chem.* **182**, 2873 (2009).
- [47] J. Wu, X. Yan, W. Guo, X. Wang, C. Yin, and X. Kuang, Molecule-like cluster magnetism and cationic order in the new hexagonal perovskite Ba₄Sn_{1.1}Mn_{2.9}O₁₂, *RSC Adv.* **11**, 40235 (2021).
- [48] L. T. Nguyen and R. J. Cava, Hexagonal perovskites as quantum materials, *Chem. Rev.* **121**, 2935 (2021).
- [49] J. W. Furness, A. D. Kaplan, J. Ning, J. P. Perdew, and J. Sun, Accurate and numerically efficient r2scan meta-generalized gradient approximation, *J. Phys. Chem. Lett.* **11**, 8208 (2020).